CHEMISTRY

# Two triplet emitting states in one emitter: Near-infrared dual-phosphorescent $Au_{20}$ nanocluster

**Wei-Dan Si[1]†, Chengkai Zhang[1]†, Meng Zhou[2], Wei-Dong Tian[1], Zhi Wang[1], Qingsong Hu[3], Ke-Peng Song[1], Lei Feng[1], Xian-Qiang Huang[4], Zhi-Yong Gao[5], Chen-Ho Tung[1], Di Sun[1]***



**Intrinsic dual-emission (DE) of gold nanoclusters in the near-infrared (NIR) are fascinating for fundamental importance and practical applications, but their synthesis remains a formidable challenge and sophisticated excited-state processes make elucidating DE mechanisms much more arduous. Here, we report an all-alkynyl–protected gold nanocluster, Au20, showing a prolate $Au_{12}$ tri-octahedral kernel surrounded by two $Au_2(CZ\text{-}PrA)_3$ dimers, four $Au(CZ\text{-}PrA)_2$ monomers, and two $CZ\text{-}PrA^-$ bridges. Au20 exhibits distinguished photophysical properties including NIR DE at 820 and 940 nm, microsecond radiative relaxation, and 6.26% photoluminescent quantum yield at ambient environment in nondegassed solution. Combining systematic studies on steady/transient spectroscopy and theoretical calculation, we identified two triplet charge transfer (CT) states, ligand-to-kernel and kernel-based CT states as DE origins. Furthermore, this NIR DE exhibits highly independent and sensitive response to surrounding environments, which well coincide with its mechanism. This work not only provides a substantial structure model to understand a distinctive DE mechanism but also motivates the further development of NIR DE materials.**

## INTRODUCTION

Near-infrared (NIR) luminescent materials have a wide range of applications in biological systems owing to their excellent penetration, less photodamage, and high signal-to-noise ratio (*1*, *2*). In particular, the intrinsic NIR dual-emission (DE) materials exhibit superior in accurate and quantitative analysis compared to single-emissive nanomaterials (*3*). Because of the simple structure and facile modification of the organic molecules, a large number of purely molecules have been found to exhibit DE, and considerable efforts have been devoted to unravel their complicated and mysterious DE mechanisms (*4*, *5*). Systematic perceptions between the dual-emissive organic molecules and the underlying photophysical processes have been proposed (*4*). However, most DE organic molecules face the limitation of short emission wavelengths; thus, it is difficult to achieve NIR DE for them.

Compared to organic molecules, atomically precise gold nanoclusters composed of inorganic metal core and organic ligand shell have structural diversity and stability, especially the large Stoke shift due to the heavy atom effects, making them promising candidates for NIR DE materials (*6*–*9*). Although a variety of gold nanoclusters exhibit unique NIR characteristic (*10*–*15*), there are rare examples of DE in NIR region (*16*). Moreover, the lack of fundamental and evidence-based understanding correlation between structure and NIR DE properties impedes the exploration of how to purposefully design and synthesize NIR DE gold nanoclusters. To date, only few impressive progresses have been made in revealing underlying NIR DE mechanism of gold nanoclusters in the recent literatures (*17*–*21*). Primitively, an intramolecular charge transfer (CT) between core and protective shell in monolayer-stabilized gold nanoclusters was proposed (*17*, *18*). Li *et al.* (*19*) deciphered that the slow process of excited-state transformation induces controllable DE behaviors in $Au_{24}(S\text{-}TBBM)_{20}$ and $Au_{14}Cd(SAdm)_{12}$ nanoclusters with bi-tetrahedral $Au_8$ core from an experimental perspective, followed by Havenridge and Aikens (*20*) who further explained the DE mechanism of $Au_{14}Cd$ using time-dependent density functional theory (TD-DFT) plus tight binding. More recently, Zhou and Song (*21*) revealed that core-shell CT state and the $Au_{13}$ core state result in visible and NIR emissions of $[Au_{25}(SR)_{18}]^-$ nanoclusters. Luo *et al.* (*16*) found that DE in $Au_{42}(PET)_{32}$ (PET = 2-phenylethanethiolate) is from first excited singlet state ($S_1$) and excited triplet state ($T_1$), between which intersystem crossing (ISC) occurs. The above cases provide well-understood explanations for the DE phenomena in thiolate-protected gold nanoclusters, but it is still undetermined whether these DE mechanisms are universally applicable to other types of gold nanoclusters, such as alkynyl-protected gold nanoclusters. Thus, obtaining suitable structure models with NIR DE properties is prerequisite to solve above question.

Here, we report a new type of NIR DE gold nanocluster, $[Au_{20}(CZ\text{-}PrA)_{16}]^{2-}$ [**Au20**; CZ-PrAH = 9-(prop-2-yn-1-yl)-9H-carbazole], which constitutes a nonclosed metal-ligand shell. It consists of a prolate $Au_{12}$ kernel fused by three $Au_6$ octahedra and two V-shaped $Au_2(CZ\text{-}PrA)_3$ "staple" motifs, four linear $Au(CZ\text{-}PrA)_2$ motifs, and two bridging $CZ\text{-}PrA^-$ ligands. Unlike other reported DE gold-thiolate nanoclusters (Fig. 1) (*16*, *19*, *21*), **Au20** exhibits not only NIR DE but also microsecond radiative relaxation and a relatively high photoluminescent quantum yield (PLQY) up to 6.26%. A systematic study of optical spectroscopy and DFT calculations revealed two triplet CT states in one nanocluster, which had

[1]School of Chemistry and Chemical Engineering, State Key Laboratory of Crystal Materials, Shandong University, Jinan 250100, People's Republic of China. [2]Hefei National Research Center for Physical Sciences at the Microscale, Department of Chemical Physics, University of Science and Technology of China, Hefei, Anhui 230026, China. [3]Hubei Key Laboratory of Low Dimensional Optoelectronic Materials and Devices, Hubei University of Arts and Science, Xiangyang 441053, China. [4]Shandong Provincial Key Laboratory of Chemical Energy Storage and Novel Cell Technology, and School of Chemistry and Chemical Engineering, Liaocheng University, Liaocheng 252000, People's Republic of China. [5]School of Chemistry and Chemical Engineering, Henan Normal University, Henan, Xinxiang 453007, People's Republic of China.
†These authors contributed equally to this work.
*Corresponding author. Email: dsun@sdu.edu.cn.

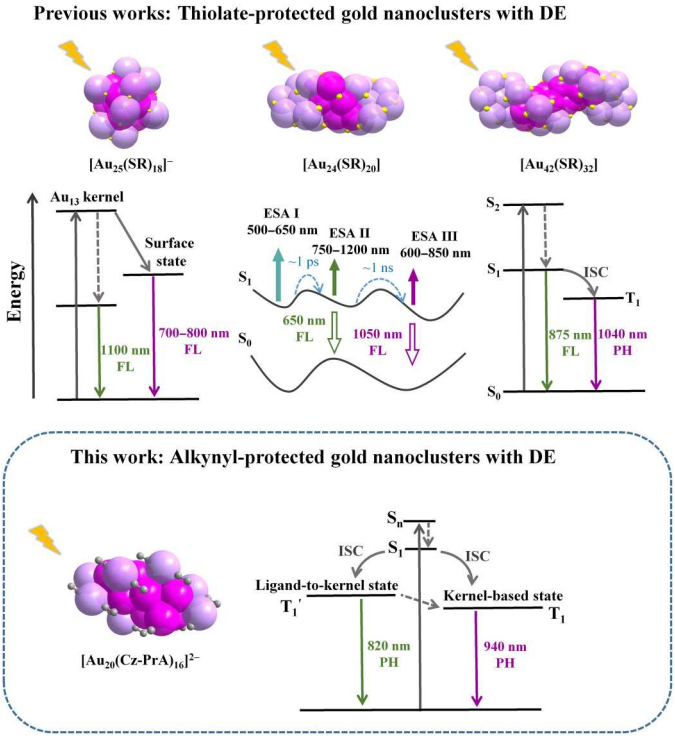


**Fig. 1. Comparisons of DE mechanisms of gold nanoclusters.** DE mechanisms of thiolate-protected $Au_{25}$, $Au_{24}$, and $Au_{42}$ nanoclusters in previous reports (*16*, *19*, *21*) and alkynyl-protected $[Au_{20}(CZ\text{-}PrA)_{16}]^{2-}$ in this work. FL, fluorescence; PH, phosphorescence.

never been observed before in Au-thiolate nanoclusters. Moreover, these two NIR emission bands exhibit different sensitive responses to the surrounding environments. This work not only sheds light on previously unknown insight into the NIR DE mechanism of gold-alkynyl nanocluster but also opens the avenues for the exploration of NIR DE gold-alkynyl nanoclusters.

## RESULTS

### Synthesis discussion

In this study, we choose CZ-PrAH as protective ligand to passivate gold kernel surface, according to our previous work (*22*). The choice of CZ-PrAH is based on the unique parent structural advantages of carbazole. (i) Nitrogen atom of carbazole is easily modified by propargyl group through nucleophilic substitution reaction to coordinate with gold atoms, thus regulating the geometric/electronic structures of nanoclusters (*23*). (ii) Carbazole and its derivatives, as a good electronic donor with a rigid π-conjugated plane and heteroatom N, are promising candidates for tuning photoluminescence (PL) properties of nanoclusters (*24*). (iii) Aromatic rings of CZ-PrAH ligands on nanoclusters surface would provide an ideal platform to establish intra- and intermolecular interactions, which play a crucial role in stabilizing nanoclusters or their packing in crystals (*25*).

Subsequently, **Au20** nanocluster was synthesized through a one-pot method as described in Fig. 2A. In brief, a mixed solution of $CH_2Cl_2$ and $CH_3OH$ containing $[Au(SMe_2)Cl]$, CZ-PrAH, and $^nBu_4NPF_6$ was directly reduced with $NaBH_4$ in the presence of triethylamine ($Et_3N$). After 3 weeks, dark green crystals were obtained by slow diffusion of *n*-hexane into the reaction solution. In the synthetic process, $^nBu_4NPF_6$ is indispensable for the whole system, providing $^nBu_4N^+$ counterions to balance the charge of nanoclusters. Because of their high disorder in the crystal lattice, $^nBu_4N^+$ counterions are difficult to be located by crystallography but have been detected by electrospray ionization mass spectrometry (ESI-MS) (vide infra).

The molecular composition and the charge state of **Au20** were further verified by ESI-MS. As shown in Fig. 2B, the spectrum shows a predominant peak at mass/charge ratio (*m*/*z*) 3603.326 (calcd. *m*/*z* 3603.319) in negative mode, corresponding to the molecular ion $[Au_{20}(CZ\text{-}PrA)_{16}]^{2-}$. The existence of $^nBu_4N^+$ counterions is confirmed by ESI-MS in positive mode (Fig. 2C). In addition, DFT studies were also performed to verify the charge state of **Au20** with the cases of anionic $[Au_{20}(CZ\text{-}PrA)_{16}]^{2-}$ and neutral $[Au_{20}(CZ\text{-}PrA)_{16}]^0$ (fig. S1). The calculated absorption spectrum of $[Au_{20}(CZ\text{-}PrA)_{16}]^{2-}$ matches well with the experimental absorption spectrum. In contrast, the calculated absorption spectrum of the $[Au_{20}(CZ\text{-}PrA)_{16}]^0$ is far different from the experimental spectrum (fig. S1B), indicating that the charge state of **Au20** is −2. Thus, the total number of free electrons of **Au20** can be determined to be 6 ($N^* = 20 + 2 - 16 = 6$), which suggests that **Au20** is a superatom with an oblate configuration of $1S^21P^4$ according to Mingos′ rule (*26*). The high-angle annular dark-field scanning transmission electron microscopy (HAADF-STEM) was performed to confirm the morphology and mono-dispersity of **Au20** in solution (fig. S2). Powder x-ray diffraction (PXRD) confirms the phase purity of bulk sample of **Au20** (fig. S3).

### X-ray crystal structure of Au20

Single-crystal x-ray diffraction analysis reveals that **Au20** crystallizes in the monoclinic space group *C*2/*c* at 100 K (table S1). The approximate dimension of the total **Au20** nanocluster is 2.3 × 1.8 × 1.8 nm, while it is about 1.3 × 0.66 × 0.66 nm when the organic shell is removed (Fig. 3, A and B). Structurally, **Au20** has a $C_i$ symmetry and is composed of a ladder-shaped $Au_{20}$ metallic framework and 16 $CZ\text{-}PrA^-$ ligands (Fig. 3). According to the "divide and protect" concept (*27*), the structure of **Au20** can be viewed as a prolate $Au_{12}$ kernel surrounded by two V-shape "CZ—$CH_2$—C≡C—Au—C≡C(—$CH_2$—CZ)—Au—C≡C—$CH_2$—CZ" dimeric "staple" motifs and four linear "CZ—$CH_2$—C≡C—Au—C≡C—$CH_2$—CZ" motifs, along with two $\mu_1$-$CZ\text{-}PrA^-$ ligands (Fig. 3, C to E, and fig. S4). The prolate $Au_{12}$ kernel can be identified as an assemble of three face-fused $Au_6$ octahedra (Fig. 3, C and D), which gives an average Au···Au distance of 2.84 Å, being 1.4% shorter as compared to that of 2.88 Å in bulk gold (*28*). Similar $Au_{12}$ trioctahedral units are also observed in the higher nuclearity gold nanoclusters, $Au_{30}(S\text{-}Adm)_{18}$ and $Au_{54}(Et_3P)_{18}Cl_{12}$ nanoclusters (*29*, *30*). Contributed by the centrosymmetric nature of **Au20**, these V-shape, linear motifs, and simple terminal ligands in a diagonal or oblique position of $Au_{12}$ are identical. With the ligation of these coordinated motifs, the Au···Au distances of the total $Au_{20}$ metallic core are obviously stretched (average, 2.97 Å).

On the periphery of the ladder-shaped $Au_{20}$ metallic core, 16 $CZ\text{-}PrA^-$ ligands display two types of coordinated modes: $\mu_2$-$\eta^1$, $\eta^2$ or σ mode (fig. S5). These alkynyl ligands adopt an anistropic

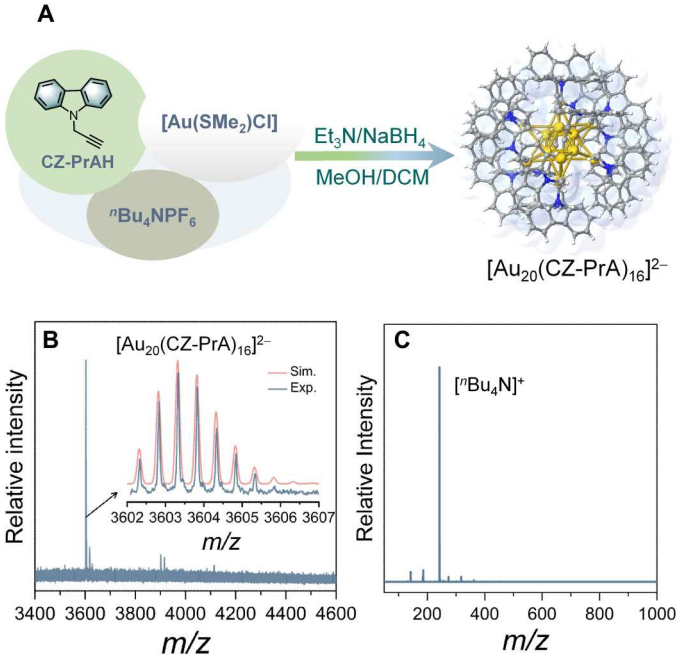


**Fig. 2. Synthesis and characterization of the Au20 nanocluster.** (**A**) Synthetic route for **Au20**. ESI-MS of **Au20** dissolved in $CHCl_3/CH_3OH$ collected in negative (**B**) and positive mode (**C**). Inset: the experimental (faint blue trace) and simulated (pink trace) isotopic patterns.

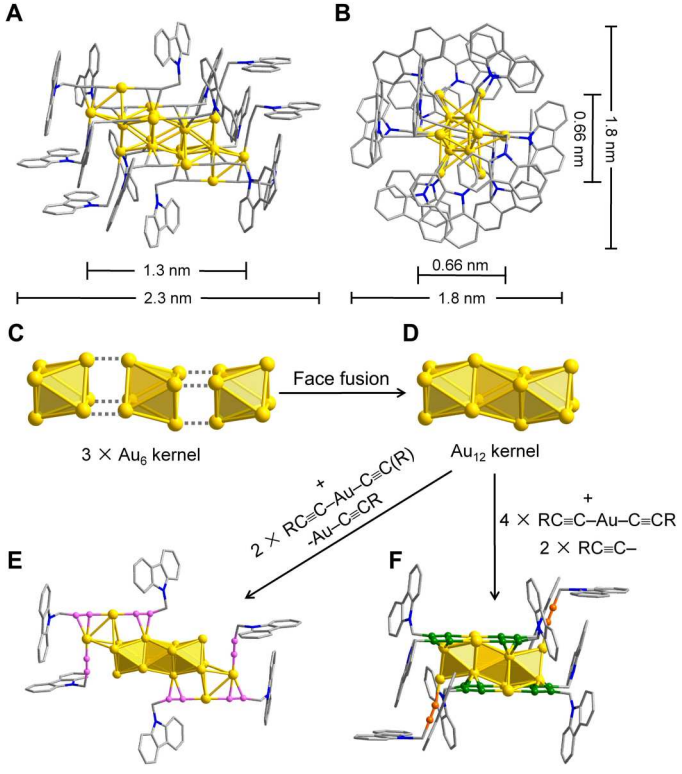


**Fig. 3. Structural anatomy of Au20.** The front (**A**) and side (**B**) views of the overall structure of **Au20**. (**C**) Three $Au_6$ octahedral kernel; (**D**) $Au_{12}$ kernel constructed by face fusion of three $Au_6$ octahedra; (**E**) The $Au_{12}$ kernel surrounded by two V-shaped RC≡C—Au—C≡C(R)—Au—C≡CR dimeric "staple" motifs. (**F**) The $Au_{12}$ kernel surrounded by four linear RC≡C—Au—C≡CR motifs and two $RC{\equiv}C^-$ ligands. R═ CZ—$CH_2$. All hydrogen atoms are omitted for clarity. Color codes: yellow, Au; blue, N; pink, green, and gray, C.

distribution based on coordinated modes. Among them, 12 CZ-$PrA^-$ take $\mu_2$-$\eta^1$,$\eta^2$ mode lying prone on the surface of the metallic core in the horizontal direction, and the remaining four CZ-$PrA^-$ are in a perpendicular arrangement on the left and right sides of ladder-shaped $Au_{20}$ through σ bonding. The Au—C bond lengths for σ bonds and π bonds fall in the range of 1.840(18) to 2.033(16) Å ($d_{avg.}$ = 1.99 Å) and 2.214(13) to 2.348(14) Å ($d_{avg.}$ = 2.28 Å), respectively. To our knowledge, it is the first time that the anistropic distribution of alkynyl ligands is observed in all-alkynyl–protected gold nanoclusters.

Such a well-organized arrangement of the CZ-$PrA^-$ ligands with large π-conjugated carbazole rings serves as an essential role in long-range ordered packing of the **Au20**. As shown in figs. S6 and S7, the close-packing diagram of **Au20** displays abundant intra- and intermolecular interactions, including noncovalent interactions and van der Waals forces. Within the individual nanocluster, offset parallel CZ-$PrA^-$ ligands engage in π···π interactions between π-conjugated carbazole rings, and C(sp3)—H···π interactions between methylene group and carbazole rings. Some carbazole rings of CZ-$PrA^-$ ligands in edge-to-face positions facilitate the formation of tilted T-shaped C(sp2)—H···π interaction (fig. S6 and S8). In addition, the methylene groups of two CZ-$PrA^-$ ligands are closed enough to the Au atoms to form intramolecular C(sp3)—H···Au interactions. In crystal lattice (fig. S7), neighboring **Au20** nanoclusters are tightly locked together via a multitude of interactions, involving tilted T-shaped edge-to-face stacking C(sp2)—H···π interactions, C(sp2)—H···Au, and H···H interactions. The abovementioned interactions are crucial for the stability and formation of crystals of **Au20**.

It is noteworthy that **Au20** has same metal-to-ligands ratio as the previously reported neutral $Au_{20}(SR)_{16}$ composed of one bi-tetrahedral $Au_7$ kernel and one giant octameric $Au_8(SR)_8$ ring, trimeric $Au_3(SR)_4$, and two monomeric $Au(SR)_2$ motifs (*31*) but exhibits completely different geometric and electronic structures. This again confirms that the different coordination mode of alkynyl and thiolate ligands have a marked influence on the molecular and electronic structures of gold nanoclusters (*32*).

## Dual emission and excitation-state dynamic of Au20

Among the various properties of gold nanoclusters, NIR PL is of great interest (*10*–*15*). Here, we systematically investigated the optical properties of **Au20** nanocluster. To ensure the high purity of samples, the **Au20** crystals were used to perform a series of optical measurements. Figure 4A displays the ultraviolet-visible (UV-vis) absorption (green) and PL (red) spectra of **Au20** in 2-methyl tetrahydrofuran (2-Me-THF) under ambient conditions. By contrast, the CZ-PrAH ligand shows an emission peak in the visible region instead of the NIR region (fig. S9) under the same test conditions. In the steady-state absorption spectrum, the solution of **Au20** shows a major absorption band at 600 nm in the low-energy region and two shoulder peaks at ~330 and 725 nm. The absorption edge at ~1.84 eV corresponds to the highest occupied molecular orbital (HOMO)–lowest unoccupied molecular orbital (LUMO) gap ($E_g$), which is consistent with electrochemical gap (1.90 eV) from differential pulse voltammetry (DPV)

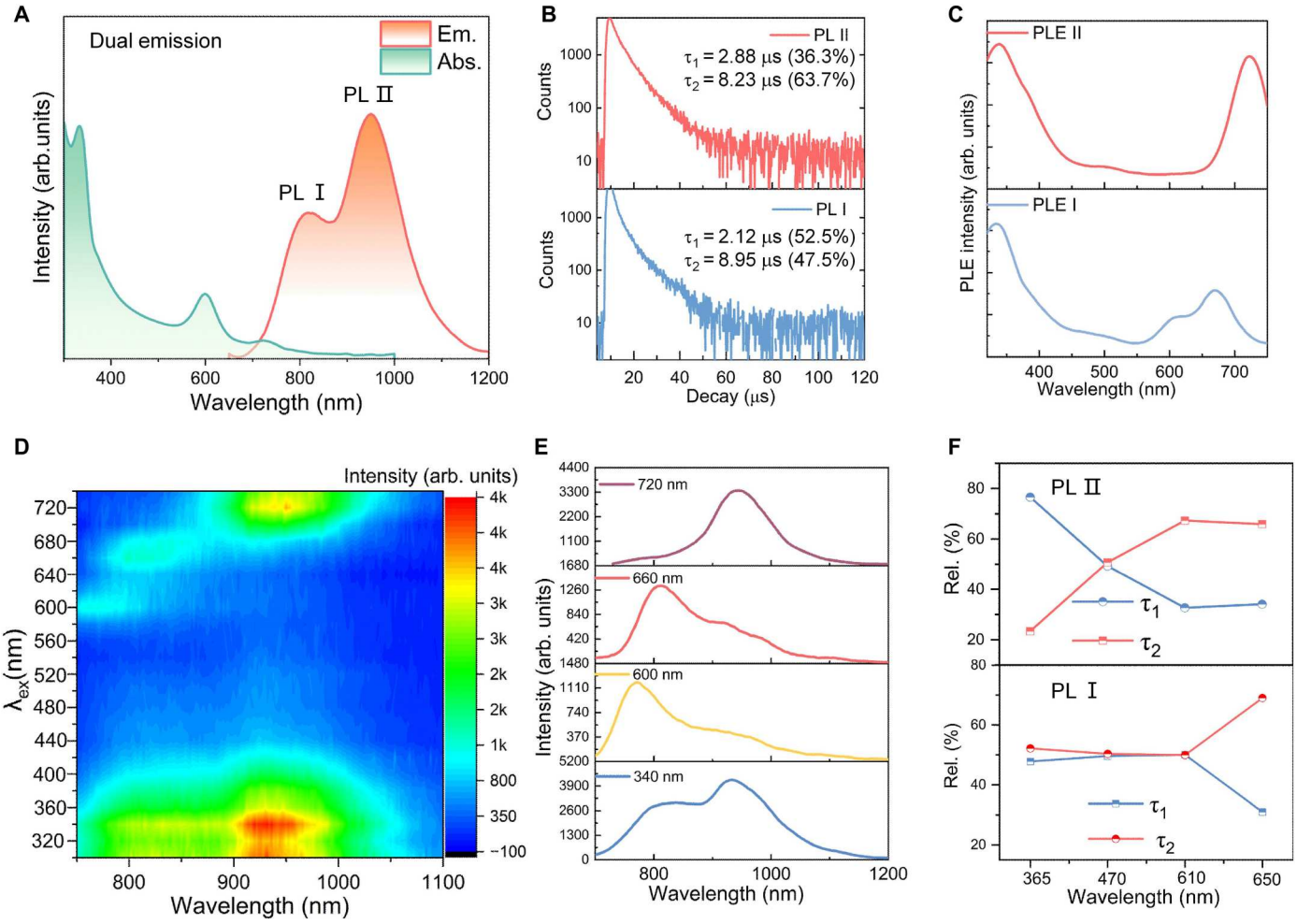


**Fig. 4. Excitation-dependent emission spectra of Au20.** (**A**) Absorption and emission spectra of **Au20** in 2-Me-THF. (**B**) Photoluminescence (PL) decay curves of 750 (PL I) and 1050 nm (PL II). (**C**) PL excitation (PLE) spectrum of **Au20** at different emission wavelength. (**D**) 2D consecutive PLE/PL map of **Au20**. (**E**) PL spectra under four selected excitation wavelengths. (**F**) Relative amplitude of the lifetime of dual emission under four excitation wavelengths.

measurement (fig. S10). In combination of the $E_g$ value and the quantum confinement effects due to the diameter approach the electron′s Fermi wavelength, this nanocluster starts to exhibit molecule-like optical transitions and NIR luminescence (*18*, *33*). Upon excitation with 365-nm UV light, **Au20** exhibits a NIR DE with two maximum wavelengths located at ~820 nm (PL I, 1.51 eV) and ~940 nm (PL II, 1.32 eV) at room temperature (Fig. 4A), with large Stocks shifts (i.e., 1239.83/820 to 1239.83/600 = 0.55 eV for PL I and 1239.83/940 to 1239.83/600 = 0.75 eV for PL II). The PLQY of **Au20** was determined to be 6.26% (Cy7.5 as standard). The PL spectra were deconvoluted into two Voigt profiles to extract the contribution from each peak, in which PL II shows a higher PLQY than PL I (1.42% for PL I and 4.84% for PL II). The DE dynamics of **Au20** were studied by time-correlated single-photon counting (TCSPC) technique. By fitting the decays of PL I and PL II, their average lifetimes are determined to be ~7.53 and 7.34 μs, respectively, manifesting that PL I and PL II should be triplet emission (decays around 750 and 1050 nm are monitored to reduce mutual interference in overlapping emission bands) (Fig. 4B and Table 1). To verify this speculation, the emission spectra of $N_2$- and $O_2$-purged solution of **Au20** were measured (fig. S11), which are identical to that of **Au20** under ambient conditions. By comparison, the emission intensities of PL I and PL II were enhanced and reduced under $N_2$ and $O_2$ atmosphere, respectively. The singlet oxygen ($^1O_2$) production is confirmed by a rapid decrease in the characteristic absorption band of 1,3-diphenyliso-benzofuran (DPBF) solution containing **Au20** (fig. S12). These results indicate that **Au20** can be used as a photosensitizer for $^1O_2$ generation, and both PL I and PL II are phosphorescence. The decay lifetime of its DE is neither like $[Au_{25}(SR)_{18}]^-$ nor like $Au_{42}(PET)_{32}$, in which the former has nanosecond-scale decay time in visible and NIR emission (*21*), while the latter gives a singlet and triplet emission with nanosecond (ns) and microsecond lifetimes, respectively (*16*). Therefore, the mechanism of kernel-shell CT and singlet/triplet states may be ruled out. Besides, such NIR dual long-lived PL bands have not been observed in any thiolate-protected gold nanoclusters.

Moreover, the PL excitation (PLE) spectra of **Au20** for emission at PL I and PL II have the same maximum excitation band located at 340 nm (Fig. 4C) but different excitation bands at low-energy region (600 and 660 nm for PL I and 720 nm for PL II.), which are not

**Table 1. PL parameters of PL I and PL II of Au20.** $\tau_{ave}$, average lifetime; $k_r$, radiative decay rate; $k_{nr}$, nonradiative decay rate; PLQY = $k_r/(k_{nr} + k_r)$; $\tau = 1/(k_{nr} + k_r)$.

| PL peak | PLQY (%) | $\tau_{ave}$ (μs) | $k_r$ ($s^{-1}$) | $k_{nr}$ ($s^{-1}$) |
|---|---|---|---|---|
| PL I | 1.42 | 7.53 | $1.89 \times 10^3$ | $1.31 \times 10^5$ |
| PL II | 4.84 | 7.34 | $6.60 \times 10^3$ | $1.30 \times 10^5$ |

consistent with its absorption spectrum. This is different obviously from previously reported $Au_{24}$(S-TBBM)$_{20}$ and $Au_{14}Cd$(SAdm)$_{12}$ nanoclusters, whose PLE and absorption spectra show a high similarity (*24*). Thus, the excited-state transformation mechanism is further excluded for NIR DE in **Au20**. To probe the underlying mechanism of NIR DE of **Au20**, we further studied the wavelength-dependence PL/PLE spectra, from which an obvious spectral difference between PL I and PL II was observed in two-dimensional (2D) PL/PLE maps (Fig. 4D). The intensity of PL I under different excitation wavelengths from 300 to 740 nm shows dynamic fluctuations and is relatively strong at three excitation wavelengths (340, 600 and 660 nm), wherein the spectra exhibit nearly single emission under the excitation of 600 and 660 nm (Fig. 4E), which is consistent with its PLE spectrum. In contrast, the intensity of PL II suffers a strongest emission at 340 and 720 nm and appears single emission under the excitation of 720 nm (Fig. 4E), which shows an entirely different trend from PL I in PL/PLE spectra. Considering the relevance between two PL bands, we deduce that two PL bands may origin from two different emitting states/centers, namely, there are two emitting states existing in one emitter (**Au20**) (*4*, *6*, *34*, *35*). Besides, the excitation-dependent decays of PL I and PL II were also performed, and their relative amplitudes of two-exponential lifetime show both the positive and negative correlation with excitation wavelength (Fig. 4F, fig. S13, and table S3), indicating that the different PL decay curves of PL I and PL II are actually combined results with different contributions from two mono-exponential decays due to the overlap of two PL bands in emission region.

In addition to the above experimental data, TD-DFT calculations were further performed to investigate the attributions of charge transition of two emitting states. Figure 5A shows the calculations of the ground states ($S_0$) of **Au20**, which gives an energy gap of 1.86 eV between the HOMO and the LUMO. The slight variation of the gap compared to those in experimental data can be attributed to the overestimation of the excitation energy by the B3LYP functional. The HOMO and LUMO orbitals of **Au20** are partially overlapping with a relatively high overlap integral ($\langle\psi_H|\psi_L\rangle$) of 0.26, in which the HOMO orbital is mainly distributed around the CZ-PrA$^-$ π* (aromatic aryl) orbitals and partly located on the Au 6sp orbitals of the outer shell of **Au20**, exhibiting typical P characters; the LUMO orbital has significant contributions from the d orbitals of Au in the ladder-shaped $Au_{12}$ kernel with a superatomic d-like character, suggesting the incorporation of ligand-to-$Au_{12}$ kernel CT (LMCT) and eight outer Au atoms to $Au_{12}$ kernel CT (MMCT) components. Four excitation states with relatively high oscillator strength, named as α, β, γ, and δ, corresponding to the four excitation wavelengths discussed above, were selected (Fig. 5B). The excitation state α is mainly contributed by the HOMO-60 ($\langle\psi_H|\psi_L\rangle$ = 0.24), HOMO-70 ($\langle\psi_H|\psi_L\rangle$ = 0.42), and HOMO-71 ($\langle\psi_H|\psi_L\rangle$ = 0.37) to LUMO orbitals transitions, in which LMCT and MMCT proportions of 59.65 and 40.34%, respectively (Fig. 5C and fig. S14). The excitation state β is mostly attributed to the HOMO-36 ($\langle\psi_H|\psi_L\rangle$ = 0.51) to LUMO orbitals transition, with small amount of the HOMO-34 ($\langle\psi_H|\psi_L\rangle$ = 0.38) to LUMO orbitals, giving LMCT and MMCT nearly the same proportions of 48.45 and 51.55%, respectively (fig. S15). The excitation state γ with the highest oscillator strength is simply involved in the transition from HOMO-36 ($\langle\psi_H|\psi_L\rangle$ = 0.51) to LUMO orbitals, with 98.44 and 1.50% for LMCT and MMCT, respectively (fig. S16). Last, the excitation state δ is ascribed to the HOMO to LUMO orbitals transition, with LMCT and MMCT proportions of 95.72 and 4.26%, respectively (Fig. 5C and fig. S17). Notably, the proportion of MMCT decreases upon wavelength varying from 368 to 615 nm and increases upon wavelength varying from 615 to 670 nm, with the lowest proportion occurring at 615 nm, which coincides with the evolution trend of PL II intensity in the 2D PLE/PL map (Fig. 4D). Meanwhile, the evolution trend in the proportion of LMCT is also coincided with that of PL I in PLE/PL map. On the basis of the above analyses, the consistency of PLE/PL map and LMCT/MMCT proportions implies that the origin of two emitting states corresponds to the two spatially separated CT states, that is, LMCT and MMCT, respectively.

To probe the excited-state dynamics of two emitting states, femtosecond (fs) and ns TA spectroscopy were performed on **Au20** in the visible region (*36*). The fs/ns-TA spectra of **Au20** pumped at 400 nm are displayed in Fig. 5D. Upon excitation with 400-nm laser pulse, rich electronic dynamics can be observed within the 20-μs time window. Three strong and net ground-state bleaching (GSB) signals around 600 (GSB I), 660 (GSB II), and 720 nm (GSB III) corresponding to the **Au20** absorption bands were observed, along with two obvious excited-state absorption (ESA) signals, ESA I and ESA II, around 500 and 675 nm in the visible range. In terms of the time-dependent evolution, within 0 to 0.15 ps, the ESA I and ESA II arise rapidly to distinct bands, and then the latter decays to nearly disappear from 0.15 to 0.4 ps. Nevertheless, the ESA I remains unchanged within 0.15 to 0.4 ps and slightly decays to a flat band more than 7 ns (Fig. 5E). Therefore, the decay of ESA II around 700 nm but no rise of ESA I at ~500 nm were observed in the early time delay due to ultrafast ISC (*37*, *38*).

The three net GSB signals keep rising in the time domain of 0 ps to 7 ns, indicating that no excited electrons decay back to the ground state in this time window. As for their evolution in ns-TA, starting from ~12 ns to 0.17 μs, there is a decrease of GSB I and GSB II center at 600 and 660 nm, respectively, accompanied by the rise of GSB III around 720 nm, suggesting the partial relaxation from one emissive state to another (Fig. 5, F and G). In combination with the 2D PL/PLE results (single emission of PL I under 600/660-nm excitations and single emission of PL II under 720-nm excitation), we proposed that the transition from the triplet CT state of PL I (T1′) to that of PL II (T1). These three GSB signals show decay time constants comparable to the microsecond lifetimes of PL bands measured by TCSPC (Fig. 5G), which indicates that the excited state undergoes very slow relaxation to the ground state to emit phosphorescence.

## DE response to multiple environment parameters

In view of the DE characteristic appearing to be sensitive to surrounding environments (*18*, *39*, *40*), we performed the PL

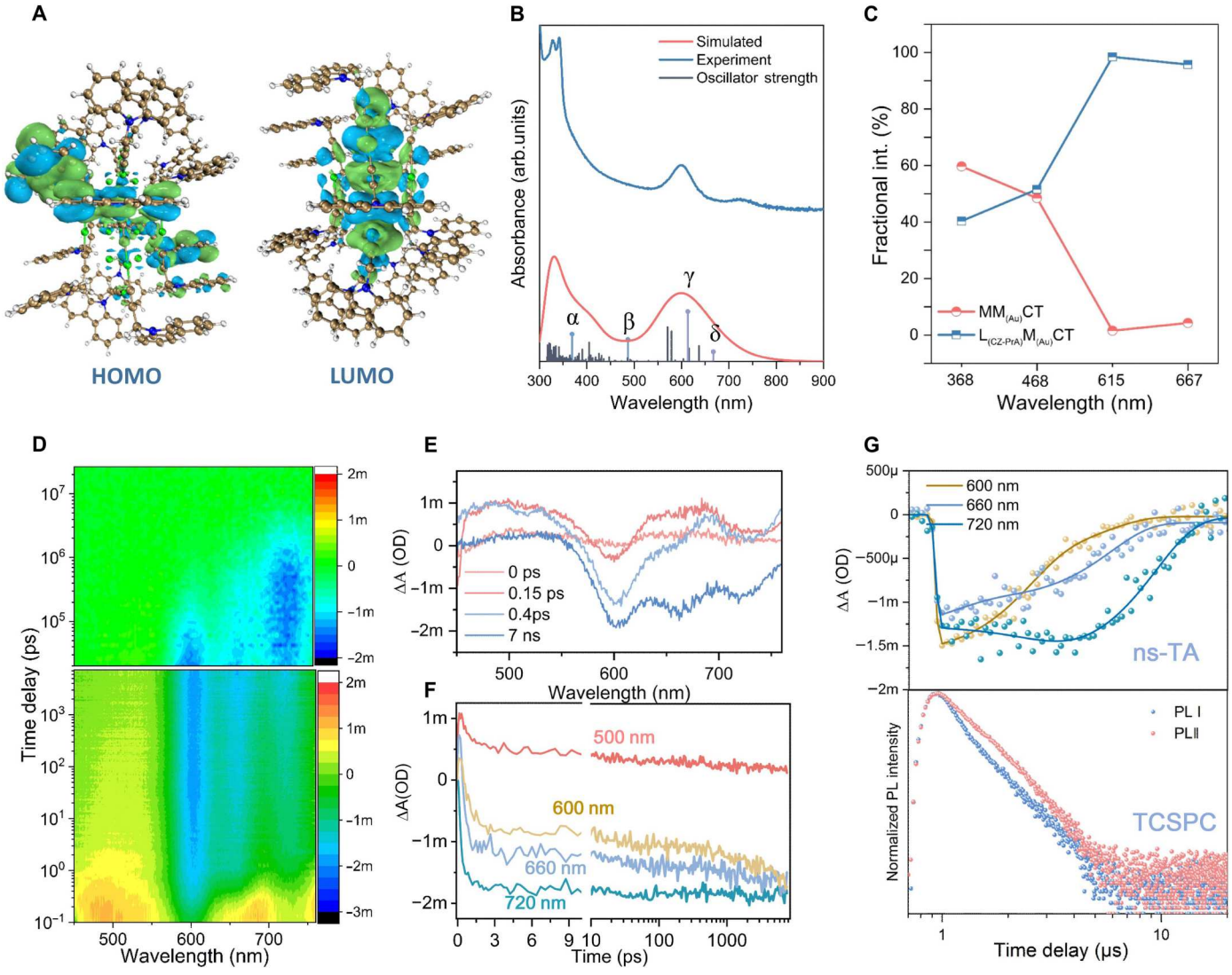


**Fig. 5. NIR DE mechanism in Au20.** (**A**) Calculated MOs (highest occupied molecular orbital, HOMO; lowest unoccupied molecular orbital, LUMO) via VMD software. (**B**) Experimental and simulated absorption spectra of **Au20**. (**C**) TD-DFT simulated fractions of charge transition at different wavelengths of **Au20** by Mulliken partition. (**D**) The fs/ns-TA map of **Au20** pumped at 400 nm. (**E**) The TA spectra of **Au20** at different time delays. (**F**) TA kinetic traces selected at specific probe wavelengths. (**G**) Comparison of the ns TA decay traces at GSB peaks and the TCSPC decay traces.

measurements of **Au20** under different temperature and polarity. First, the temperature-dependent PL spectra of **Au20** in 2-MeTHF were recorded as shown in Fig. 6A. The PL I and PL II peaks both become sharper with different degrees of blue shift upon decreasing the temperature from 293 to 113 K, indicating a strong electron-phonon interaction (Fig. 6B) (*41*). Intriguingly, the PL I and PL II give different response speeds as the temperature decreases, along with a similar intensity at 113 K. The integrated intensities of PL I and PL II were found to increase by 5.65 and 2.03 times from 293 to 113 K, respectively. Furthermore, the data fitting and peak deconvolution for all temperature-dependent spectra were performed to estimate quantificationally the contributions of PL I and PL II to the total peak (fig. S18 and table S4). It is obvious that the percentage of PL I increased from 19% at 293 K to 56% at 113 K, indicating that PL I is more susceptible to the low temperature due to the suppression of nonradiative relaxation. To study the nonradiative relaxation process of DE bands in **Au20**, the quantitative temperature-dependent intensity evolutions for DE peaks are plotted. As shown in Fig. 5C, the curves of PL intensity of PL I and PL II versus temperature can be fitted (PL intensity at 113 K as unity) to analyze the thermally activated nonradiative relaxation pathway (single dominant nonradiative channel using Arrhenius expression (Eq. 1) (*42*)

$$I(T) = \frac{I_0}{1 + ae^{-E_a/K_B T}} \quad (1)$$

where $a$ is the ratio of nonradiative and radiative probabilities and $E_a$ is the activation energy of the nonradiative relaxation channel. The activation energies of acoustic phonon modes coupled with PL I and PL II are determined to be around 23.6 meV (23.6 meV × 8.0 $cm^{-1}$/meV = 188.8 $cm^{-1}$) and 15.3 meV (15.3 meV × 8.0 $cm^{-1}$/meV = 122.4 $cm^{-1}$), respectively. The

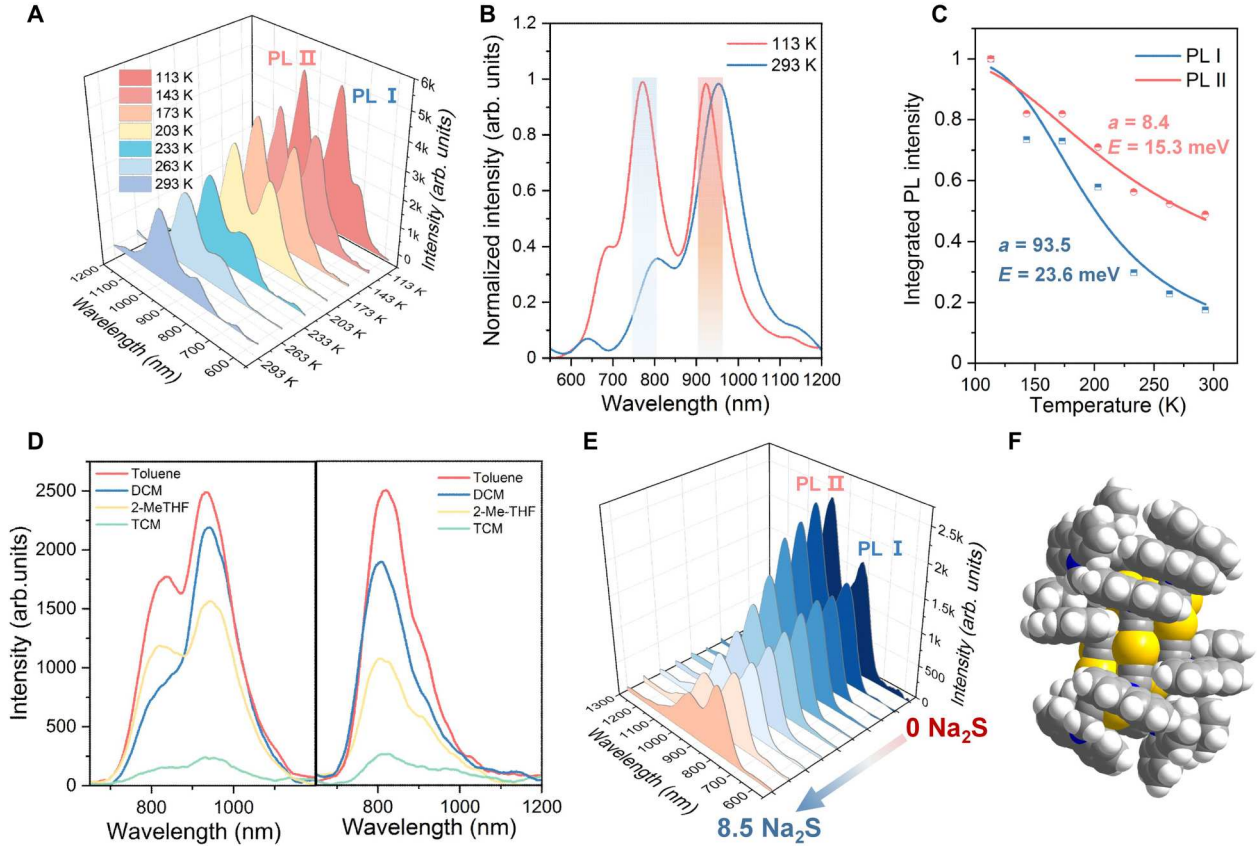


**Fig. 6. DE response to multiple environment parameters.** (**A**) Variable-temperature PL spectra of **Au20** in 2-Me-THF. (**B**) Normalized spectra at 113/293 K. (**C**) Normalized integrated PL I and II peak intensities and fitting using Eq. 1 (data from variable-temperature PL spectra of **Au20**). (**D**) Solvent polarity dependence PL spectra of **Au20** at the excitation of 365 nm (left) and 600 nm (right). (**E**) PL titration experiments of **Au20** at varying $Na_2S$ concentration. (**F**) The space-filling structure of **Au20**.

possible origin of low-frequency phonon mode (<150 $cm^{-1}$) of PL II is the Au-Au vibration of metallic kernel in **Au20**, while the relatively higher phonon mode of PL I may be assigned to the Au-C vibration in shell of **Au20** (*43*, *44*). Such a result also reflects the nature of DE of **Au20**. Specifically, the PL I arises from the ligand-to-kernel CT state; thus, it is more easily affected by the low temperature for the suppression of nonradiative relaxation. Conversely, the PL II is contributed by the kernel-based CT state, which exhibits less affected by the low temperature. In addition, this result also indicates that **Au20** can be used as a ratiometric temperature probe for noncontact optical thermometry (*45*, *46*). Of note, the lifetimes of PL I and PL II both show mono-exponential in the 233 to 113 K region, revealing that only a single emitting state exists in each PL band, which is most likely due to the minimal overlapping of the two PL bands in low temperature (figs. S19 and S20 and table S5).

Next, given that the solvent-dependent effects can lead to a perturbation of the NIR DE of **Au20** (*18*), the NIR PL spectra of **Au20** were measured in four organic solvents of different polarity (TCM, 2-Me-THF, DCM, and toluene) with a same concentration under excitation at 365 nm and 600 nm. Different from the PL properties of $Au_{24}$(S-TBBM)$_{20}$ with polarity dependence of one of the DE peaks due to the CT nature in both PL states, two emission bands in **Au20** almost exhibit independent responses to polarity since the DE characteristic of **Au20** involved with two triple CT states in one nanocluster. As shown in Fig. 6D, under excitation at 365 nm, as the polarity decreases from the higher-polarity TCM to the lower-polarity toluene, a obvious increase was observed for the intensities of both PL I and PL II, among which the PL I exhibited a broad band in TCM and DCM, and a relatively sharp peak in 2-Me-THF and toluene, while all the PL II retained a sharp peak in these four solvents. To exclude the interference of PL II on PL I, the excitation wavelength was converted to 600 nm to record the PL spectra of **Au20**. As anticipated, only PL I appeared and showed a similar increasing trend with the change of solvent polarity. The UV-vis absorption spectra and the PL lifetime of **Au20** in different solvents show a same character, indicating no change in the ground state and decay time of electron-hole recombination (figs. S21 and S22 and Table S6). Therefore, the polar environment could induce polarization to the excited states from two triplet CT states, leading to the change of emission (*39*, *47*–*49*). To further elucidate the effects of polar environment on the excited state of kernel, the titration experiment of $Na_2S$ was carried out. As shown in Fig. 6E, the emission intensity of PL I and PL II decrease immediately even when 0.5 equivalents of $Na_2S$ was added. Upon adding more $Na_2S$, the emission intensity of PL spectra continued declining, with the decrease of PL II being more distinct from that of PL I. After the addition of 5.5 equivalents of $Na_2S$, the PL II almost disappeared, while PL I remained unchanged. These results not only reveal that the existence of bare Au site on **Au20** surface can be more susceptible to

$S^{2-}$ bonding (Fig. 6F) but also validate that the polar environment can make an effect on the excited state of kernel. In summary, the independent dual responses to the temperature/polarity/$Na_2S$ concentration provide further evidence that the mechanism of NIR DE arises from two triplet emitting states, which indicates that **Au20** is a potential ratiometric probe.

## DISCUSSION

In summary, we successfully isolated an all-alkynyl–protected gold nanocluster, **Au20**, by introducing carbazole-based CZ-PrAH ligand. **Au20** has a prolate tri-octahedral $Au_{12}$ kernel encaged by a nonclosed metal-ligand shell. Impressively, **Au20** demonstrates an extraordinary intrinsic DE in NIR region and a microsecond radiative relaxation with PLQY of 6.26%. The comprehensive analysis of optical spectra and DFT calculations confirmed that the DE of **Au20** origins from two triplet CT states, including ligand-to-kernel and kernel-based transitions. To our knowledge, this is also the first time to decipher the DE mechanism in alkynyl-protected gold nanoclusters. In addition, these two emissions are highly sensitive to temperature, polarity, etc., and give different responses. This work provides a vital structure model to exploit a previously unknown explanation for atomically precise nanoclusters with DE phenomena, and the unique property of **Au20** is encouraging and will promote its development for practical optoelectronic, ratiometric sensing, and biomedical applications in the future.

## MATERIALS AND METHODS

### Synthesis of Au20

[$Au(SMe_2)Cl$] (6 mg, 0.02 mmol), CZ-PrAH (4.5 mg, 0.022 mmol), and $^{n}Bu_4NPF_6$ (7.6 mg, 0.02 mmol) were dissolved in 3 ml of $CH_2Cl_2$, to which 10 μl of $Et_3N$ was added. After the mixture was stirred for 10 min, a freshly prepared solution of $NaBH_4$ (0.1 mg in 1 ml of $CH_3OH$) was added dropwise with the color of solution changing from pale green to dark green and finally, to green black. The reaction mixture was further stirred for 12 hours. After filtration, the filtrate was subject to the diffusion of *n*-hexane vapor to afford black rod-liked crystals after about 1 month (yield, 16.5% based on Au).

### Characterization of Au20

Mass spectra were recorded on a Bruker impact II high-definition mass spectrometer, quadrupole and time-of-flight modules both in the negative and positive ion modes. Typical measurement conditions are as follows: end plate offset = 500 V, dry gas = 4 liter/min, nebulizer = 0.3 bar, capillary voltage = 4000 V, sample flow rate = 500 μl/hour, and collision gas, $N_2$. The reported *m*/*z* values represent monoisotopic mass of the most abundant peak within the isotope pattern. The data analyses of mass spectra were performed on the basis of the isotope distribution patterns using Compass Data Analysis software (version 4.4). UV-vis absorption spectra were recorded on a Thermo Fisher Scientific Evolution 220 UV-vis spectrophotometer. Fourier transform infrared spectrum were recorded on a Bruker Tensor II spectrophotometer (Bruker Optics GmbH, Ettlingen, Germany) using a single attenuated total reflectance accessory covering a wave number range from 400 to 4000 $cm^{-1}$. The final spectrum was the average of 32 scans accumulated using Bruker's Opus software 8.1, taken at 4-$cm^{-1}$ resolution. The samples were measured under the same mechanical force pushing the samples in contact with the diamond window. PXRD analyses were carried out on a microcrystalline powder using a Rigaku Oxford Diffraction XtaLAB Synergy-S diffractometer using Cu radiation (λ = 1.54184 Å). The PXRD patterns were processed with the CrysAlisPro software suite (*50*) using the Powder function. Morphology of the sample and elemental composition analyses were measured using an SU-8010 field emission scanning electron microscope (Hitachi Ltd., Tokyo, Japan) equipped with an Oxford-Horiba Inca XMax50 energy-dispersive x-ray spectroscopy (EDS) attachment (Oxford Instruments Analytical, High Wycombe, England). The HAADF-STEM experiments were carried out at 300 kV using a double Cs-corrected FEI Themis Z microscope. The **Au20** was dissolved with $CHCl_3$ and deposited on a carbon support grid by drop-casting. The sample was dried naturally in ambient environment before measurement. DPV of **Au20** was conducted on an electrochemical work station model CHI-660E with a standard three-electrode system (glassy carbon working, Pt wire auxiliary, and $Ag/Ag^+$ reference); this study was performed on $CHCl_3$ solution containing 0.1 M $^{n}Bu_4NPF_6$ as supporting electrolyte in $N_2$ atmosphere at −5°C.

### Steady-state PL

The near-infrared (NIR) PL, PLE spectra, and quantum yield were recorded on an Edinburgh spectrofluorimeter (FLS920) using a time-correlated single-photon counting technique.

### Detection of singlet oxygen ($^1O_2$) generation

DPBF was used to detect the $^1O_2$ generation by **Au20**. In brief, DPBF in ethanol was prepared, to which the 2-Me-THF solution of **Au20** was added to give final concentrations of 1 mM for DPBF and $3.5 \times 10^{-2}$ μM for **Au20**. The mixed solution was irradiated by Xe lamp, and the adsorption spectra were recorded on a Thermo Fisher Scientific Evolution 220 UV-vis spectrophotometer.

### Transient absorption analyses

Samples were prepared by dissolving **Au20** in 2-Me-THF and transferred to a 2-mm path length quartz cuvette. An Astrella Ti:Sapphire laser system from Coherent was used as a light source, which operates at a 1-kHz repetition rate, generating 70-fs pulses at 800 nm. The ~70-fs pump laser pulse was generated by a regenerative amplifier system and the optical parametric amplifier (Coherent, Solo). A small portion of the laser fundamental was focused into a sapphire plate to produce a supercontinuum in the visible range, which overlapped with the pump in time and space. Multiwavelength transient spectra were recorded at different pump-probe delay times (Helios Fire, Ultrafast Systems). Time zero, solvent response, and chirp corrections were used using software supplied by Ultrafast Systems. Details of the x-ray crystallographic analysis and DFT calculations are provided in the Supplementary Materials.

## Supplementary Materials

**This PDF file includes:**

Supplementary Materials and Methods
Figs. S1 to S25
Tables S1 to S6
References

## REFERENCES AND NOTES


1. H. Liu, G. Hong, Z. Luo, J. Chen, J. Chang, M. Gong, H. He, J. Yang, X. Yuan, L. Li, X. Mu, J. Wang, W. Mi, J. Luo, J. Xie, X.-D. Zhang, Atomic-precision gold clusters for NIR-II imaging. *Adv. Mater.* **31**, 1901015 (2019).
2. Y. Cai, Z. Wei, C. Song, C. Tang, W. Han, X. Dong, Optical nano-agents in the second near-infrared window for biomedical applications. *Chem. Soc. Rev.* **48**, 22–37 (2019).
3. H. Ma, J. Wang, X.-D. Zhang, Near-infrared II emissive metal clusters: From atom physics to biomedicine. *Coord. Chem. Rev.* **448**, 214184 (2021).
4. S. K. Behera, S. Y. Park, J. Gierschner, Dual emission: Classes, mechanisms, and conditions. *Angew. Chem. Int. Ed.* **60**, 22624–22638 (2021).
5. N. A. Kukhta, M. R. Bryce, Dual emission in purely organic materials for optoelectronic applications. *Mater. Horiz.* **8**, 33–55 (2021).
6. Z. Liu, Z. Wu, Q. Yao, Y. Cao, O. J. H. Chai, J. Xie, Correlations between the fundamentals and applications of ultrasmall metal nanoclusters: Recent advances in catalysis and biomedical applications. *Nano Today* **36**, 101053 (2021).
7. I. Chakraborty, T. Pradeep, Atomically precise clusters of noble metals: Emerging link between atoms and nanoparticles. *Chem. Rev.* **117**, 8208–8271 (2017).
8. M. R. Narouz, S. Takano, P. A. Lummis, T. I. Levchenko, A. Nazemi, S. Kaappa, S. Malola, G. Yousefalizadeh, L. A. Calhoun, K. G. Stamplecoskie, H. Häkkinen, T. Tsukuda, C. M. Crudden, Robust, highly luminescent $Au_{13}$ superatoms protected by N-heterocyclic carbenes. *J. Am. Chem. Soc.* **141**, 14997–15002 (2019).
9. C. M. Aikens, Electronic and Geometric structure, optical properties, and excited state behavior in atomically precise thiolate-stabilized noble metal nanoclusters. *Acc. Chem. Res.* **51**, 3065–3073 (2018).
10. Y. Song, J. Zhong, S. Yang, S. Wang, T. Cao, J. Zhang, P. Li, D. Hu, Y. Pei, M. Zhu, Crystal structure of $Au_{25}(SePh)_{18}$ nanoclusters and insights into their electronic, optical and catalytic properties. *Nanoscale* **6**, 13977–13985 (2014).
11. X.-K. Wan, W. W. Xu, S.-F. Yuan, Y. Gao, X.-C. Zeng, Q.-M. Wang, A near-infrared-emissive alkynyl-protected $Au_{24}$ nanocluster. *Angew. Chem. Int. Ed.* **54**, 9683–9686 (2015).
12. G. Li, H. Abroshan, C. Liu, S. Zhuo, Z. Li, Y. Xie, H. J. Kim, N. L. Rosi, R. Jin, Tailoring the electronic and catalytic properties of $Au_{25}$ nanoclusters via ligand engineering. *ACS Nano* **10**, 7998–8005 (2016).
13. J. Wang, Z.-Y. Wang, S.-J. Li, S.-Q. Zang, T. C. W. Mak, Carboranealkynyl-protected gold nanoclusters: Size conversion and UV/Vis-NIR optical properties. *Angew. Chem. Int. Ed.* **60**, 5959–5964 (2021).
14. Q. Li, C. J. Zeman, Z. Ma, G. C. Schatz, X. W. Gu, Bright NIR-II photoluminescence in rod-shaped icosahedral gold nanoclusters. *Small* **17**, 2007992 (2021).
15. Q. Li, C. J. Zeman, G. C. Schatz, X. W. Gu, Source of bright near-infrared luminescence in gold nanoclusters. *ACS Nano* **15**, 16095–16105 (2021).
16. L. Luo, Z. Liu, X. Du, R. Jin, Near-infrared dual emission from the $Au_{42}(SR)_{32}$ nanocluster and tailoring of intersystem crossing. *J. Am. Chem. Soc.* **144**, 19243–19247 (2022).
17. D. Lee, R. L. Donkers, G. L. Wang, A. S. Harper, R. W. Murray, Electrochemistry and optical absorbance and luminescence of molecule-like $Au_{38}$ nanoparticles. *J. Am. Chem. Soc.* **126**, 6193–6199 (2004).
18. M. Zhou, S. Vdović, S. Long, M. Zhu, L. Yan, Y. Wang, Y. Niu, X. Wang, Q. Guo, R. Jin, A. Xia, Intramolecular charge transfer and solvation dynamics of thiolate-protected $Au_{20}(SR)_{16}$ clusters studied by ultrafast measurement. *J. Phys. Chem. A* **117**, 10294–10303 (2013).
19. Q. Li, D. Zhou, J. Chai, W. Y. So, T. Cai, M. Li, L. A. Peteanu, O. Chen, M. Cotlet, X. Wendy Gu, H. Zhu, R. Jin, Structural distortion and electron redistribution in dual-emitting gold nanoclusters. *Nat. Commun.* **11**, 2897 (2020).
20. S. Havenridge, C. M. Aikens, Deciphering the dual emission in the photoluminescence of $Au_{14}Cd(SR)_{12}$: A theoretical study using TDDFT and TDDFT + TB. *J. Chem. Phys.* **155**, 074302 (2021).
21. M. Zhou, Y. Song, Origins of visible and near-infrared emissions in $[Au_{25}(SR)_{18}]^-$ nanoclusters. *J. Phys. Chem. L* **12**, 1514–1519 (2021).
22. C. Zhang, Z. Wang, W.-D. Si, L. Wang, J.-M. Dou, Z.-Y. Gao, C.-H. Tung, D. Sun, Solvent-induced isomeric $Cu_{13}$ nanoclusters: Chlorine to copper charge transfer boosting molecular oxygen activation in sulfide selective oxidation. *ACS Nano* **16**, 9598–9607 (2022).
23. M. Bashir, A. Bano, A. S. Ijaz, B. A. Chaudhary, Recent developments and biological activities of N-substituted carbazole derivatives: A review. *Molecules* **2015**, 13496–13517 (2015).
24. H. Zhang, H. Ma, W. Huang, W. Gong, Z. He, G. Huang, B. S. Li, B. Z. Tang, Controllable room temperature phosphorescence, mechanoluminescence and polymorphism of a carbazole derivative. *Mater. Horiz.* **8**, 2816–2822 (2021).
25. X. Zhang, L.-Y. Zhang, J.-Y. Wang, F.-R. Dai, Z.-N. Chen, Two-step phosphorescent mechanochromism due to intramolecular deformation. *J. Mater. Chem. C* **8**, 715–720 (2020).
26. D. M. P. Mingos, Structural and bonding patterns in gold clusters. *Dalton Trans.* **44**, 6680–6695 (2015).
27. H. Häkkinen, M. Walter, H. Grönbeck, Divide and protect: Capping gold nanoclusters with molecular gold–Thiolate rings. *J. Phys. Chem. B* **110**, 9927–9931 (2006).
28. H. Schmidbaur, A. Schier, Aurophilic interactions as a subject of current research: An update. *Chem. Soc. Rev.* **41**, 370–412 (2012).
29. T. Higaki, C. Liu, C. Zeng, R. Jin, Y. Chen, N. L. Rosi, R. Jin, Controlling the atomic structure of $Au_{30}$ nanoclusters by a ligand-based strategy. *Angew. Chem. Int. Ed.* **55**, 6694–6697 (2016).
30. S. Kenzler, C. Schrenk, A. Schnepf, $Au_{54}(Et_3P)_{18}Cl_{12}$: A structurally related cluster to $Au_{32}(Et3P)_{12}Cl_8$ gives insight into the formation process. *Dalton Trans.* **49**, 10765–10771 (2020).
31. C. Zeng, C. Liu, Y. Chen, N. L. Rosi, R. Jin, Gold–thiolate ring as a protecting motif in the $Au_{20}(SR)_{16}$ nanocluster and implications. *J. Am. Chem. Soc.* **136**, 11922–11925 (2014).
32. Z.-J. Guan, F. Hu, J.-J. Li, Z.-R. Wen, Y.-M. Lin, Q.-M. Wang, Isomerization in alkynyl-protected gold nanoclusters. *J. Am. Chem. Soc.* **142**, 2995–3001 (2020).
33. S. Mustalahti, P. Myllyperkiö, S. Malola, T. Lahtinen, K. Salorinne, J. Koivisto, H. Häkkinen, M. Pettersson, Molecule-like photodynamics of $Au_{102}(pMBA)_{44}$ nanocluster. *ACS Nano* **9**, 2328–2335 (2015).
34. A. P. Demchenko, V. I. Tomin, P.-T. Chou, Breaking the kasha rule for more efficient photochemistry. *Chem. Rev.* **117**, 13353–13381 (2017).
35. T. Itoh, Fluorescence and phosphorescence from higher excited states of organic molecules. *Chem. Rev.* **112**, 4541–4568 (2012).
36. Q. Li, M. Zhou, W. Y. So, J. Huang, M. Li, D. R. Kauffman, M. Cotlet, T. Higaki, A. L. Peteanu, Z. Shao, R. Jin, A mono-cuboctahedral series of gold nanoclusters: Photoluminescence origin, large enhancement, wide tunability, and structure–Property correlation. *J. Am. Chem. Soc.* **141**, 5314–5325 (2019).
37. Y. Li, Y. Song, X. Zhang, T. Liu, T. Xu, H. Wang, D.-E. Jiang, R. Jin, Atomically precise $Au_{42}$ nanorods with longitudinal excitons for an intense photothermal effect. *J. Am. Chem. Soc.* **144**, 12381–12389 (2022).
38. S.-S. Zhang, S. Havenridge, C. Zhang, Z. Wang, L. Feng, Z.-Y. Gao, C. M. Aikens, C.-H. Tung, D. Sun, Sulfide boosting near-unity photoluminescence quantum yield of silver nanocluster. *J. Am. Chem. Soc.* **144**, 18305–18314 (2022).
39. M. Glasbeek, H. Zhang, Femtosecond studies of solvation and intramolecular configurational dynamics of fluorophores in liquid solution. *Chem. Rev.* **104**, 1929–1954 (2004).
40. J. Zhu, X. Song, L. Gao, Z. Li, Z. Liu, S. Ding, S. Zou, Y. He, A highly selective sensor of cysteine with tunable sensitivity and detection window based on dual-emission Ag nanoclusters. *Biosens. Bioelectron.* **53**, 71–75 (2014).
41. M. S. Devadas, S. Bairu, H. Qian, E. Sinn, R. Jin, G. Ramakrishna, Temperature-dependent optical absorption properties of monolayer-protected $Au_{25}$ and $Au_{38}$ clusters. *J. Phys. Chem. Lett.* **2**, 2752–2758 (2011).
42. J. A. Steele, P. Puech, B. Monserrat, B. Wu, R. X. Yang, T. Kirchartz, H. Yuan, G. Fleury, D. Giovanni, E. Fron, Role of electron–phonon coupling in the thermal evolution of bulk rashba-like spin-split lead halide perovskites exhibiting dual-band photoluminescence. *ACS Energy Lett.* **4**, 2205–2212 (2019).
43. Z. Liu, Y. Li, W. Shin, R. Jin, Observation of core phonon in electron–phonon coupling in $Au_{25}$ nanoclusters. *J. Phys. Chem. Lett.* **12**, 1690–1695 (2021).
44. M. Kato, Y. Shichibu, K. Ogura, M. Iwasaki, M. Sugiuchi, K. Konishi, I. Yagi, Terahertz raman spectroscopy of ligand-protected Au8 clusters. *J. Phys. Chem. Lett.* **11**, 7996–8001 (2020).
45. R. Kawagoe, I. Takashima, S. Uchinomiya, A. Ojida, Reversible ratiometric detection of highly reactive hydropersulfides using a FRET-based dual emission fluorescent probe. *Chem. Sci.* **8**, 1134–1140 (2017).
46. F. Vetrone, R. Naccache, A. Zamarrón, A. J. de la Fuente, F. Sanz-Rodríguez, L. Martinez Maestro, E. Martín Rodriguez, D. Jaque, J. García Solé, J. A. Capobianco, Temperature sensing using fluorescent nanothermometers. *ACS Nano* **4**, 3254–3258 (2010).
47. L.-Y. Yao, V. W.-W. Yam, Dual emissive gold(I)–sulfido cluster framework capable of benzene–cyclohexane separation in the solid state accompanied by luminescence color changes. *J. Am. Chem. Soc.* **143**, 2558–2566 (2021).
48. A. Rosspeintner, B. Lang, E. Vauthey, Ultrafast photochemistry in liquids. *Annu. Rev. Phys. Chem.* **64**, 247–271 (2013).
49. V. D. Thanthirige, E. Sinn, G. P. Wiederrecht, G. Ramakrishna, Unusual solvent effects on optical properties of bi-icosahedral $Au_{25}$ clusters. *J. Phys. Chem. C* **121**, 3530–3539 (2017).
50. Rigaku Oxford Diffraction. *CrysAlis$^{Pro}$ Software system, version 1.171.40.25a*, Rigaku Corporation, (2018).
51. L. Palatinus, G. Chapuis, SUPERFLIP–A computer program for the solution of crystal structures by charge flipping in arbitrary dimensions. *J. Appl. Cryst.* **40**, 786–790 (2007).
52. G. M. Sheldrick, Crystal structure refinement with SHELXL. *Acta Crystallogr. C* **71**, 3–8 (2015).
53. O. V. Dolomanov, L. J. Bourhis, R. J. Gildea, J. A. K. Howard, H. Puschmann, OLEX2: A complete structure solution, refinement and analysis program. *J. Appl. Cryst.* **42**, 339–341 (2009).
54. A. L. Spek, Structure validation in chemical crystallography. *Acta. Crystallogr. Sect. D* **65**, 148–155 (2009).

55. M. J. Frisch, G. W. Trucks, H. B. Schlegel, G. E. Scuseria, M. A. Robb, J. R. Cheeseman, G. Scalmani, V. Barone, G. A. Petersson, H. Nakatsuji, X. Li, M. Caricato, A. V. Marenich, J. Bloino, B. G. Janesko, R. Gomperts, B. Mennucci, H. P. Hratchian, J. V. Ortiz, A. F. Izmaylov, A.F. Sonnenberg, J. L. Williams-Young, D. Ding, F. Lipparini, F. Egidi, F. Goings, J. Peng, B. Petrone, A. Henderson, T. Ranasinghe, D. Zakrzewski, V. G. Gao, J. Rega, N. Zheng, G. Liang, W. Hada, M. Ehara, M. Toyota, K. Fukuda, R. Hasegawa, J. Ishida, M. Nakajima, T. Honda, Y. Kitao, O. Nakai, H. Vreven, T. Throssell, K. Montgomery Jr., J. A. Peralta, J. E. Ogliaro, F. Bearpark, M. J. Heyd, J. J. Brothers, E.N. Kudin, K. N. Staroverov, V. N. Keith, T. A. Kobayashi, R. Normand, J. Raghavachari, K. Rendell, A. P. Burant, J. C. Iyengar, S. S. Tomasi, J. Cossi, M. Millam, J. M. Klene, M. Adamo, C. Cammi, R. Ochterski, J. W. Martin, R. L. Morokuma, K. Farkas, O. Foresman, J. B. Fox, D. J. Gaussian, Gaussian 16, Rev. B.01, Gaussian, Inc.: Wallingford, CT (2016). M. J. Frisch,G. W. Trucks,H. B. Schlegel,G. E. Scuseria, M. A. Robb, J. R. Cheeseman,G. Scalmani, V. Barone, G. A. Petersson, H. Nakatsuji, X. Li, M. Caricato, A. V. Marenich, J. Bloino, B. G. Janesko, R. Gomperts, B. Mennucci, H. P. Hratchian, J. V. Ortiz, A. F. Izmaylov, J. L. Sonnenberg,Williams, F. Ding, F. Lipparini, F. Egidi, J. Goings, B. Peng, A. Petrone, T. Henderson, D. Ranasinghe, V. G. Zakrzewski, J. Gao, N. Rega, G. Zheng, W. Liang, M. Hada, M. Ehara, K. Toyota, R. Fukuda, J. Hasegawa, M. Ishida, T. Nakajima, Y. Honda, O. Kitao, H. Nakai, T. Vreven, K. Throssell, J. A. Montgomery Jr., J. E. Peralta, F. Ogliaro, M. J. Bearpark, J. J. Heyd, E. N. Brothers, K. N. Kudin,V. N. Staroverov, T. A. Keith, R. Kobayashi, J. Normand, K. Raghavachari, A. P. Rendell, J. C. Burant, S. S. Iyengar, J. Tomasi, M. Cossi, J. M. Millam, M. Klene, C. Adamo, R. Cammi, J. W. Ochterski, R. L. Martin, K. Morokuma, O. Farkas, J. B. Foresman, D. J. Fox, Gaussian16: RevisionA.03, Gaussian, Inc. (2016).

56. T. Lu, F. Chen, Multiwfn: A multifunctional wavefunction analyzer. *J. Comput. Chem.* **33**, 580–592 (2012).

57. E. R. Johnson, S. Keinan, P. Mori-Sánchez, J. Contreras-García, A. J. Cohen, W. Yang, Revealing noncovalent interactions. *J. Am. Chem. Soc.* **132**, 6498–6506 (2010).

58. J. Contreras-García, E. R. Johnson, S. Keinan, R. Chaudret, J.-P. Piquemal, D. N. Beratan, W. Yang, NCIPLOT: A program for plotting noncovalent interaction regions. *J. Chem. Theor. Comput.* **7**, 625–632 (2011).

**Acknowledgments:** We thank the Analytical Center for Structural Constituent and Physical Property of Core Facilities Sharing Platform, Shandong University for Femtosecond transient absorption spectroscopy system. **Funding:** This work was financially supported by the National Natural Science Foundation of China (grant nos. 52261135637, 22201159, 22150410333, and 22171164), the Natural Science Foundation of Shandong Province (nos. ZR2019ZD45 and ZR2020ZD35), the Taishan Scholar Project of Shandong Province of China (nos. tsqn201812003 and ts20190908), the National Postdoctoral Innovative Talents Support Program (no. BX2021171), and China Postdoctoral Science Foundation (no. 2021M700081). **Author contributions:** D.S. conceived and designed the experiments; W.-D.S. and C.Z. conducted synthesis, characterization, and analyzed data; W.-D.S., C.Z., M.Z., and D.S. contributed to scientific discussion; W.-D.T. and Z.W. assisted in synthesis; Q.H., L.F., K.-P.S., X.-Q.H., and Z.Y.G. assisted in the measurements; C.-H.T. and D.S. supervised the manuscript; W.-D.S., C.Z., and D.S. wrote the paper. All authors discussed the results and commented on the manuscript. **Competing interests:** The authors declare that they have no competing interests. **Data and materials availability:** All data needed to evaluate the conclusions in the paper are presented in the paper and/or the Supplementary Materials. The cif. data of **Au20** can be obtained free of charge from The Cambridge Crystallographic Data Centre (CCDC). CCDC 2222330.

Submitted 18 December 2022
Accepted 1 March 2023
Published 29 March 2023
10.1126/sciadv.adg3587